Preprint: P. Fang, B. Wang, C. P. Mulligan, T. M. Murray, S. V. Khare, D. Gall, "Epitaxial growth of cubic WC_y(001) on MgO(001)," J. Alloys Compd. **860**, 158403 (2020). http://dx.doi.org/10.1016/j.jallcom.2020.158403

Epitaxial growth of cubic WC_y(001) on MgO(001)

Peijiao Fang,[1] Baiwei Wang,[1] C. P. Mulligan,[2] T. M. Murray,[3] S. V. Khare,[4] Daniel Gall[1]

[1] *Department of Materials Science and Engineering, Rensselaer Polytechnic Institute, Troy, NY 12180, USA*
[2] *U.S. Army Combat Capabilities Development Command, Armaments Center, Benét Laboratories, Watervliet, NY 12189, USA*
[3] *Colleges of Nanoscale Science & Engineering, SUNY Polytechnic Institute, Albany, NY 12203, USA*
[4] *Department of Physics and Astronomy, University of Toledo, Toledo, OH 43606, USA*

Tungsten carbide films are sputter-deposited onto MgO(001) substrates at 400 °C in 5 mTorr Ar - CH_4 gas mixtures with CH_4 fractions f_{CH4} = 0.4% - 6%, yielding total C-to-W ratios x = 0.57 - 1.25 as determined by ion beam analyses and energy-dispersive X-ray spectroscopy. The C-to-W ratio y in the cubic WC_y phase is smaller than x, ranging from y = 0.47 to 0.68, as determined from lattice constant a_o measurements in combination with first-principle calculations that predict an increasing $a_o = (0.4053 + 0.0295y)$ nm for y = 0.3-1.0. This suggests that the cubic phase is stabilized by carbon vacancies and that the layers contain amorphous C with a volume fraction increasing from 4% - 26% for f_{CH4} = 0.4% - 6%. X-ray diffraction (XRD) ω-2θ scans, ω-rocking curves, and reciprocal space maps in combination with high-resolution transmission electron microscopy (TEM) indicate the growth of epitaxial rock-salt structure WC_y(001) layers with a cube-on-cube epitaxial relationship with the substrate: $(001)_{WC} \parallel (001)_{MgO}$ and $[100]_{WC} \parallel [100]_{MgO}$. The measured XRD out-of-plane coherence length of 8 – 14 nm is nearly independent of the film thickness d = 10 or 600 nm, suggesting that growth beyond d = 10 nm leads to an epitaxial breakdown and the nucleation of misoriented hexagonal or orthorhombic W_2C grains for $f_{CH4} \leq 1\%$ and cubic nanocrystalline WC_y grains for $f_{CH4} > 1\%$.
Keywords: tungsten carbide, epitaxy, x-ray diffraction, hard coating, vacancy, sputter deposition

I. Introduction

Transition metal carbides and nitrides are well-known for their high hardness, chemical inertness, thermal stability, and promising electrochemical properties, and are therefore commercially used as protective, wear-resistant and decorative coatings [1-3] and diffusion barrier layers in microelectronics [4], and are widely studied as potential electrodes and catalysts for electrochemical energy storage and conversion systems [5-7], as electrical contacts [8, 9], as superconductive layers [10] and as coatings for biomedical components [11]. The coating properties are typically strongly affected by the microstructure including grain size [12, 13] and orientation distribution [14, 15], phase and composition variations [14-17], surface roughness [18], stress [19] and porosity [14, 15, 18, 19]. Therefore, controlling the microstructural development during layer deposition is important to achieve desired properties but requires an understanding of the growth kinetics. Epitaxial layer growth represents a model system to study growth kinetics and, in addition, also provides phase-pure single-orientation grain-boundary-free samples which are ideal to measure the intrinsic properties without confounding microstructural effects. Correspondingly, a considerable body of work exists on the growth of epitaxial transition metal nitrides including ScN [20], TiN [21, 22], VN [23], CrN [24-26], NbN [27], MoN [28], HfN [29], TaN [30], and WN [31]. In contrast, much less is known about on the epitaxial growth of transition metal carbides with a few reports on sputter deposition of TiC(001) [32], $(V_{1-x}Cr_x)_2C$(0001) [33],

NbC_xN_{1-x}(001) [34], ZrC [35] and MoC_x(001) [36], the use of evaporated C_{60} as the carbon source to deposit epitaxial TiC, VC, NbC, MoC, W_2C and WC [37], and a somewhat larger number of studies on epitaxial growth of MAX phase carbides [38, 39].

Tungsten carbide is commercially used as the major constituent in cemented carbide cutting tools owing to its high hardness, wear resistance, and stability to thermal shock [1, 40-42]. In addition, tungsten carbide has been reported to exhibit Pt-like catalytic properties [43] and is therefore used as electrochemical catalyst for the hydrogen evolution reaction (HER) [7, 44, 45], substituting more expensive noble metals. Tungsten carbide crystalizes in three phases [1]: (i) stoichiometric hexagonal δ-WC in which both tungsten and carbon sublattices form a simple hexagonal structure and carbon occupies the trigonal-prismatic interstitial site of the metal sublattice, (ii) cubic B1 NaCl structure γ-WC_y which exhibits a relatively large composition range y = 0.59-1.00 that is facilitated by vacancies on anion sites as is characteristic for under-stoichiometric carbides [46, 47], and (iii) hexagonal tungsten semi-carbide W_2C in which W forms a hcp sublattice and C occupies half of the octahedral interstitial sites with different arrangements dependent on the temperature, yielding four polymorphs: β''-, β'-, β- and ε-W_2C [46, 48, 49]. Distinction between the W_2C polymorphs by X-ray diffraction (XRD) is typically not feasible because the reflections from the W hcp lattice are identical for all four polymorphs and peaks associated with ordering on the anion sites are small, due to the small scattering cross section for C [46]. Hexagonal WC is the only thermodynamically stable carbide at room temperature, while W_2C and cubic WC_y become stable at $T > 1523$ and 2789 K, respectively. Nevertheless, sputter-deposited tungsten carbide films typically consist of a mixture of metastable W_2C, cubic WC_y, and amorphous carbon (a-C), while the hexagonal WC phase is absent, suggesting kinetic barriers for its formation [40-42, 50, 51]. Most thin film studies on tungsten carbide focus on improving its mechanical properties for hard wear-resistant coatings [40-42], with others reporting on optical and electrical [52], or catalytic properties [44, 45]. Few studies report on the epitaxial tungsten carbide growth including epitaxial hexagonal WC(0001) films deposited on W(110) substrates by plasma-enhanced chemical vapor deposition [53], single crystal cubic WC_y(001) and (111) films deposited using a fullerene carbon source [54], and epitaxial W_2C(0001) Schottky contacts formed during annealing of W films on 4H-SiC substrates [55].

In this paper, we report on the epitaxial growth of cubic WC_y(001) on MgO(001) substrates by reactive DC magnetron sputtering from a W target in 5 mTorr Ar/CH_4 gas mixtures at 400 °C. A combination of XRD and transmission electron microscopy (TEM) analyses indicate a critical thickness of approximately 10 nm for the epitaxial breakdown where the microstructure transitions from epitaxial cubic WC_y(001) to nanocrystalline WC_y with inclusions of W_2C grains for deposition at low CH_4 partial pressures, and a secondary amorphous carbon phase a-C:H, where ":H" denotes the possible hydrogenation of the amorphous carbon phase [56]. First-principles simulations provide values for the predicted lattice constant vs C-vacancy concentration which are used in combination with the measured relaxed lattice constants to quantify the relative C distribution in the cubic WC_y and a-C:H phases from the measured total C-to-W ratio x.

II. Procedure

All WC_x layers were deposited in a load-locked ultra-high vacuum (UHV) DC magnetron sputtering system with a base pressure of 10^{-9} Torr [57, 58]. Single-side polished 10 × 10 × 0.5 mm^3 epitaxial MgO(001) substrates were successively cleaned in ultrasonic baths of trichloroethylene, acetone, isopropyl alcohol, and deionized water for 20 min each; blown dry with nitrogen; mounted onto a Mo holder via silver paint; and inserted into the deposition system

through the load-lock chamber. The substrates were degassed in vacuum for 1h at 1000 °C using a radiative pyrolytic graphite heater. Subsequently, the temperature was reduced to 400 °C, as measured by a thermocouple below the sample stage. The sputter target was a 5-cm-diameter, 0.6-cm-thick 99.95% pure W disk positioned 9 cm from a continuously rotating substrate at a 45° tilt. The target was sputter etched for 5 min prior to each deposition with a shutter shielding the substrate. 99.999% pure Ar, which was further purified with a MicroTorr purifier, and 99.999% pure CH_4 were introduced into the deposition chamber through needle valves to reach a constant total pressure of 5 mTorr, while varying the CH_4 fraction f_{CH4} from 0.4% to 6%. A constant DC power of 120 W applied to the tungsten target yielded a tungsten carbide deposition rate that decreases slightly and monotonically with increasing f_{CH4} from 11 to 10 nm/min. Two sample sets with nominal thicknesses of d = 10 and 600 nm were deposited using deposition times of 1.0 and 60.0 min, respectively. The thickness measured by X-ray reflectivity (XRR) and cross-sectional scanning electron microscopy (SEM) is 10.5 ± 0.5 nm for the thin layers and between 650 and 750 nm for the thick layers, in reasonable agreement with the deposition rate estimates which do not account for x-dependent density variations.

X-ray diffraction including reciprocal space mapping (RSM) was done using a Panalytical X'pert PRO MPD system with a Cu source and a hybrid mirror with a two-bounce two-crystal Ge(220) monochromator, yielding a parallel incident beam with a wavelength $\lambda_{K\alpha 1}$ = 1.5406 Å and a divergence of 0.0068°. Direct beam alignment, sample height adjustment, as well as correction of the substrate ω and χ tilt angles were performed prior to all scans. Symmetric ω-2θ scans were obtained using a 0.04 rad Soller slit in front of a PIXcel solid-state line detector operated in receiving mode with a 0.165 mm active length, effectively acting as a point detector. ω rocking curves were acquired with the same parallel beam geometry using a constant 2θ angle corresponding to the WC_y 002 reflection. ϕ-scans were performed to align the sample with regards to its in-plane rotation prior to performing asymmetric RSMs around 113 reflections. RSM scans were done by taking advantage of all 256 channels of the solid state line detector and using a small diffracted beam exit angle ~10° with respect to the sample surface to cause beam narrowing which increases the 2θ resolution. In addition, symmetric ω-2θ scans with a Bragg-Brentano divergent beam geometry were collected over a large 2θ = 5-85° range in order to detect small inclusions of possible secondary phases or misoriented grains. Grazing incidence XRD scans were collected with a parallel beam geometry using an X-ray mirror (< 0.055° divergence), a line detector with a 0.165 mm active length, and a constant incidence angle ω = 1° and 10° for d = 10 and 600 nm, respectively, which are both above the critical angle of tungsten carbide and were chosen to maximize the thin film peak intensity while ensuring that diffracted intensity is detected from the whole layer thickness.

Energy-dispersive X-ray spectroscopy (EDS) analyses were done in a FEI Helios Nanolab SEM operated with a 5.0 kV accelerating voltage and a 5.0 mm working distance. An Oxford Instruments X-Max^N 80 silicon drift detector that is particularly well suited for light element detection was used to obtain the spectra that were analyzed with the Oxford Instruments AZtec EDS software. We expect the compositional accuracy for the WC_x specimens to be ±4 atomic percentage of carbon, which corresponds to a 18% uncertainty in the C-to-W ratio, based on test measurements on a SiC standard using the same detector. Rutherford backscattering spectrometry (RBS) and elastic (non-Rutherford) backscattering spectrometry (EBS) were conducted using a 4.35 MeV $^4He^+$ ion beam incident at an angle of 6° relative to the sample surface normal, and a total scattering angle of 166° between the incident beam and the detector. The beam energy was

chosen 0.09 MeV above the resonance energy of 4.26 MeV for elastic scattering on carbon atoms, yielding a maximum scattering cross-section that is more than two orders of magnitude larger than the $^4He^+$ reflection from C atoms for conventional Rutherford scattering [59]. This maximum scattering on C atoms occurs approximately 200 nm below the top surface, after the $^4He^+$ ions have lost 0.09 MeV of their initial energy, assuming a 4×10^2 MeV/mm stopping power. The W and C atomic areal densities were determined from RBS and EBS spectra using the SIMNRA simulation software [60].

Transmission electron microscopy (TEM) was done in a 300 kV FEI Titan^3 microscope equipped with a probe corrector, monochromator, Bruker SuperX EDS detector, and a Gatan Imaging Filter (GIF). The specimens were prepared by cleaving them into $2 \times 1 \times 0.5$ mm^3 cuboids and attaching them onto a glass slide for mechanical polishing to reach a cross-sectional thickness of approximately 100 μm. Subsequently, they were transferred onto a focused ion beam (FIB) holder and electron transparent lamella were prepared by FIB milling in a FEI Versa 3D DualBeam instrument, using a final polishing step at 5 kV to minimize ion beam damage.

First-principles calculations were performed using the Vienna *ab initio* simulation package (VASP), employing periodic boundary conditions, a plane wave basis set, the Perdew-Burke-Ernzerhof generalized gradient approximation exchange correlation functional revised for solids (PBEsol) [61], and the projector-augmented wave method [62]. An energy convergence of < 1 meV/atom was achieved with a 600 eV cut-off energy for the plane-wave basis set and Γ-centered *k*-point grids with 16×16×16, 12×12×12, 16×16×6, and 8×8×8 k-points for 2-, 8-, 12-, and 16-atom supercells, respectively. W 5*s*, 5*p*, 5*d*, and 6*s* electrons were explicitly calculated using the W_sv pseudo potential provided with the VASP package. The lattice constant of cubic WC_y was determined by removing C atoms from supercells and iteratively relaxing atomic positions and the cell-volume while keeping the cell shape fixed, such that an overall cubic structure is retained for direct comparison with experiment. Different C-vacancy arrangements were computed, in particular (a) regular 3D arrays of equally-spaced C-vacancies with $y = 0.875$ and 0.75, (b) an array of lines of C-vacancies along a close-packed [110] directions with $y = 0.75$, (c) an array of C-vacancies on alternating (001) planes with $y = 0.5$, and (d) C-vacancies on (111) planes with $y = 0.833$, 0.667, 0.5, and 0.333.

We note that the calculated formation energy per atom for stoichiometric cubic WC is 0.22 eV, but is -0.23 eV for the stable hexagonal WC phase, as calculated using PBEsol (while the standard PBE functional yields 0.31 and -0.14 eV, respectively). The positive and negative values indicate that cubic WC is unstable against decomposition into the elemental standard states, bcc W and graphite, while hexagonal WC is stable. Introducing C-vacancies in cubic WC reduces the carbide formation energy, suggesting that C-vacancies stabilize the rocksalt structure, similar to what has been reported for WN and MoN [28, 63-66]. The calculated C vacancy formation energy ranges from -2.0 to -0.8 eV, depending on configuration, but is never sufficient to decrease the formation energy below that of hexagonal WC, which remains the most stable WC phase. We have also calculated configurations with W vacancies in cubic WC_y, to explore compositions with $y > 1$. However, the W-vacancy formation energy is positive for all explored configurations, such that W vacancies are unlikely to form and are not discussed any further within this manuscript.

III. Results

Figure 1 is a plot of the measured C-to-W ratio x as a function of the methane fraction f_{CH4} in Ar-CH_4 gas mixtures during reactive sputter deposition of WC_x layers. Here, the total C-to-W ratio x includes contributions from both the cubic WC_y and other secondary phases, as discussed

below. The blue data points are obtained using energy-dispersive x-ray spectroscopy (EDS) from layers with a 600 nm nominal thickness and f_{CH4} ranging from 0.4 to 6%. The two magenta circles at f_{CH4} = 2 and 6% are from the same samples, but measured using ion beam analysis (RBS and EBS). A typical RBS/EBS spectrum from the WC_x film deposited at f_{CH4} = 6% is shown in the inset. The measured backscattered $^4He^+$ intensity is plotted as red data points while the green line is obtained from curve fitting. The spectrum exhibits a plateau at E = 3.57-4.05 MeV from Rutherford backscattering at the tungsten nuclei, a shoulder at 1.1 MeV indicating the onset of C backscattering events leading to a carbon resonance peak at E = 0.940 MeV, onsets due to Mg and O in the substrate at 1.8 and 1.1 MeV, and a feature at 0.7 MeV which is attributed to a combination of an O resonance and the minimum energy E = 0.62 MeV for backscattering from C atoms at the bottom of the layer. Curve fitting of the WC_x/MgO stacked layer structure requires only two fitting parameters, which are the area densities of W and C atoms and are determined to be 2.53×10^{18} and 3.05×10^{18} at/cm^2, respectively. This yields a C-to-W ratio $x = 1.21 \pm 0.02$, which is in good agreement (3% deviation) with $x = 1.25 \pm 0.22$ from the EDS measurements. Similarly, the RBS/EBS analysis from the film deposited at f_{CH4} = 2% yields $x = 0.77 \pm 0.01$, in reasonable agreement with $x = 0.89 \pm 0.15$ from the EDS measurements. The plotted C-to-W ratio determined by EDS increases nearly linearly from x = 0.57 to 0.69, 0.89, 1.08 to 1.25 with f_{CH4} = 0.4%, 1%, 2%, 4% and 6%. We attribute the over-stoichiometric compositions for the C-rich layers to amorphous carbon inclusions, as discussed in more detail below, and note that this data does not provide direct insight into the C-incorporation pathways, which may include reactive $CH_{x<4}$ fragments that form in the plasma or on the target surface and incorporate in the growing layer. The RBS/EBS data indicates that the tungsten areal density $\rho_W = 2.53 \times 10^{18}$ atoms/cm^2 in the layer with f_{CH4} = 6% is 22% smaller than $\rho_W = 3.25 \times 10^{18}$ atoms/cm^2 for f_{CH4} = 2%. This suggests a 22% lower tungsten sputtering rate which we attribute to a larger fraction of the W target being covered with carbon and adsorbed CH_x and/or to a reduced sputtering rate due to the larger fraction or the lighter CH_4^+ ions impinging on the target surface in comparison to the heavier Ar^+ ions. This argument is consistent with an increase in the target voltage from 344 to 386 V which, operated in constant power mode, yields a decreasing ion current with increasing f_{CH4} = 2% to 6%.

Figure 2 shows x-ray diffraction results from WC_x/MgO(001) layers with thickness d = 10 and 600 nm deposited with f_{CH4} = 0.4% - 6%. The θ-2θ patterns in Fig. 2(a) are from 10-nm-thick WC_x layers and are obtained for a narrow 2θ = 40 - 45° range using a high-resolution XRD optics yielding a monochromatic parallel beam x-ray source (see section II for details) in order to detect the 002 reflections from epitaxial WC_y near the intense MgO 002 substrate peak. For clarity purposes, the plotted intensities are offset vertically by 100, 350, 900, 1650 and 1900 cps for the layers grown with f_{CH4} = 0.4%, 1%, 2%, 4% and 6%, respectively, and the linear y-scale is chosen to display the weak WC_y 002 reflections but, correspondingly, the 10^3 times more intense MgO 002 substrate reflections at 2θ = 42.909° extend above the vertical range of the figure. The layer with f_{CH4} = 0.4% exhibits a relatively low intensity WC_y 002 peak at 2θ = 43.51° with a full width at half maximum (FWHM) of $\Gamma_{2\theta} = 1.0 \pm 0.1°$. The peak position is to the right of the substrate, indicating an out-of-plane lattice constant $a_\perp$ = 0.4157 nm that is smaller than that of the substrate a_{MgO} = 0.4212 nm, as discussed in detail below. However, as the methane content during deposition is increased to f_{CH4} = 1%, the WC_y 002 peak shifts towards the substrate peak. The pattern indicates a peak at 2θ = 42.6° which is hard to accurately locate due to the overlap with the substrate. It also exhibits a secondary feature at 2θ = 43.13° which is attributed to epitaxial WC_y growth on top of a secondary domain of the MgO substrate, consistent with the reciprocal space map results discussed below. Increasing f_{CH4} to 2%, 4% and 6% causes the WC_y 002 peak to shift further to

the left to 2θ = 42.32°, 42.35° and 42.21°, respectively, while its width $\Gamma_{2\theta}$ = 0.91 ± 0.05°, 1.2 ± 0.1° and 1.3 ± 0.1° remains approximately constant.

Fig. 2(b) shows θ-2θ patterns from WC_x/MgO(001) layers deposited with the same five methane fractions f_{CH4} = 0.4%, 1%, 2%, 4% and 6%, but with a 60 times larger thickness d = 600 nm. The XRD measurements are done under identical conditions and x- and y-axis scales are identical to those in Fig. 2(a), such that the plotted patterns in (a) and (b) can be quantitatively compared. The patterns in the two figures strongly resemble each other. More specifically, the WC_y 002 peak positions in Fig. 2(b) at 2θ = 43.29, 42.6, 42.51, 42.31 to 42.09° match those in Fig. 2(a) with < 0.5% deviation. More interestingly, the peak intensities are also similar: For example, the WC_y 002 peak intensities for d = 10 and 600 nm layers are 190 and 170 cps for f_{CH4} = 0.4% and 540 and 640 cps for f_{CH4} = 2% after normalization with the MgO 002 peak intensity. That is, the peak intensity detected by the high resolution XRD optics is identical (within ±25%) for the two sample sets, despite the 60-fold change in the layer thickness. This suggests that the majority of the 600-nm-thick layer does not contribute to the WC_y 002 peaks in Fig. 2(b), but consists of misoriented and/or alternate phase grains, as discussed below. In addition, the peak widths $\Gamma_{2\theta}$ = 0.98 ± 0.05°, 0.7 ± 0.1°, 0.87 ± 0.03°, 0.92 ± 0.03°, 1.16 ± 0.09° for d = 600 nm closely match the range $\Gamma_{2\theta}$ = 1.0 – 1.3° for d = 10 nm. These peak widths are directly used to calculate the out-of-plane x-ray coherence length $\xi_\perp = \lambda / (\Gamma_{2\theta}\cos\theta)$, which is plotted in Fig. 2(c) as a function of f_{CH4} = 0.4 - 6% for both d = 10 and 600 nm as pink and blue diamonds, respectively. This coherence length represents the out-of-plane mosaicity or incoherency of thin films and therefore corresponds to the film thickness or the height (along the growth direction) of single crystal blocks separated by crystalline defects or grain boundaries. The plotted $\xi_\perp$ = 9.5 ± 0.8, 12 ± 9, 10.4 ± 0.6, 8.2 ± 0.9 and 7.3 ± 0.7 nm for 10-nm-thick layers deposited with f_{CH4} = 0.4%, 1%, 2%, 4% and 6%, respectively. These values are in good agreement (<10 % deviation) with those determined from reciprocal space maps on the same samples, plotted in Fig. 2(c) as ×-symbols. The $\xi_\perp$ values are similar for all five d = 10 nm layers, with the largest $\xi_\perp$ for f_{CH4} = 1%, which corresponds to the sample with the smallest lattice-mismatch with the substrate. Thus, the maximum in $\xi_\perp$ may be attributed to an improved crystalline quality due to the small misfit strain. However, the uncertainty in $\xi_\perp$ for this sample is particularly large, due to the overlap of the layer and substrate peaks in Fig. 2(a). Thus, considering the experimental uncertainty, we find no strong dependence of $\xi_\perp$ on f_{CH4}, but note that all measured $\xi_\perp$ values are close to the nominal film thickness of d = 10 nm. This suggests that the physical boundaries, i.e., the film surface and the film/substrate interface, are the limiting factors for the out-of-plane coherency while crystalline defects are negligible. The corresponding vertical coherence lengths for the 600-nm-thick layers are 9.7 ± 0.5, 14 ± 2, 10.9 ± 0.4, 10.3 ± 0.3, 8.2 ± 0.7 nm for f_{CH4} = 0.4%, 1%, 2%, 4% and 6%, respectively. The blue ×-symbol in Fig. 2(c) indicates $\xi_\perp$ = 9.8 ± 0.6 nm determined from the reciprocal map of the f_{CH4} = 6% film. These $\xi_\perp$ values from d = 600 nm layers are nearly identical to those for d = 10 nm, and also show a maximum for f_{CH4} = 1% which may be attributed to the smallest lattice misfit. The agreement in the coherence length for d = 10 and 600 nm indicates that the two sample sets have the same epitaxial thickness, suggesting that only the bottom 8 - 14 nm of the 600-nm-thick layers are epitaxial, while the remainder of the layers consist of misoriented grains and/or other tungsten carbide or carbon phases, consistent with the results from Figs. 2(a) and (b). This is discussed in more detail in section IV.

Fig. 2(d) shows representative XRD rocking curves from the 002 WC_y reflections of layers with f_{CH4} = 2% and d = 10 and 600 nm. They are obtained by measuring the reflected intensity as

a function of the incident angle ω while keeping 2θ fixed at the values corresponding to the peak positions measured with the θ-2θ scans in Figs. 2(a) and (b). The plotted peaks have FWHM widths Γ_ω = 0.05 and 0.04° for d = 10 and 600 nm, respectively. Corresponding measurements are done for all samples presented in this study, indicating $\Gamma_\omega < 0.12°$ for all WC_y 002 peaks and a corresponding in-plane x-ray coherence length $\xi_\parallel = \lambda / (2\,\Gamma_\omega \sin\theta)$ ranging from 100 - 300 nm. This indicates excellent crystallinity, as the measured Γ_ω is smaller than what has been reported for most other epitaxial layers deposited on MgO(001), with Γ_ω = 0.18 - 3.3° for epitaxial fcc and bcc metals like Cu, Ag, W, Ni [67-71], and Γ_ω = 0.24 - 3.12° for rock-salt structure nitrides including ScN, TiN, CrN, NbN, MoN, HfN, TaN, WN, $Cr_{1-x}Al_xN$, $Ti_{1-x}Mg_xN$, and $Sc_{1-x}Al_xN$ [20, 22, 25, 27, 29, 31, 72-75]. We note that the MgO substrates exhibit small-angle grain boundaries which result in measured Γ_ω = 0.017 - 0.044° for the MgO 002 peaks. This represents a considerable fraction (15 - 37%) of the Γ_ω for the WC_y 002 peaks, indicating that some of the broadening in ω is due to substrate effects such that $\xi_\parallel$ is likely even larger than stated above.

Divergent-beam x-ray diffraction θ-2θ powder scans are employed to detect possible secondary phases and grain orientations that differ from the epitaxial WC_y detected in Figs. 2(a) and (b). Patterns with 2θ = 5° to 85° (not shown) exhibit only MgO 002 and WC_y 002 peaks for all samples with d = 10 nm, indicating a negligible density of misoriented grains or secondary phases for d = 10 nm. In contrast, the powder scans from 600-nm-thick layers show additional peaks from W_2C for $f_{CH4} \leq 1\%$, while layers grown with $f_{CH4} \geqslant 2\%$ result in 111, 220 and 311 WC_y peaks that indicate misoriented grains of the cubic phase. This is explored in more detail using grazing incidence x-ray diffraction (GIXRD) methods. Fig. 2(e) shows GIXRD 2θ patterns over 2θ = 5 - 85° for WC_x films with d = 600 nm and f_{CH4} = 0.4 - 6%. They are obtained using a constant incidence angle ω = 10° which results in an approximate x-ray penetration depth of 700 nm. For clarity purposes, the scans are offset vertically. The f_{CH4} = 0.4% film shows $10\bar{1}0$, $10\bar{1}1$ and $11\bar{2}0$ reflections from the W_2C phase. Here we use, for simplicity, peak labeling according to the hexagonal W_2C polymorph since, as described in the Section I, all W_2C polymorphs exhibit the same W sublattice and typically cannot be distinguished by XRD due to the low C atomic scattering factor. The relative peak intensities for W_2C $10\bar{1}0$, $10\bar{1}1$ and $11\bar{2}0$ reflections are 100:8:15, which is distinctly different from the reported 25:100:14 for randomly oriented polycrystalline W_2C (JCPDS 35-0776), suggesting a textured microstructure which may be attributed to grain nucleation on the epitaxial WC_y(001) underlayer. This is consistent with a feature at 2θ = 37.9° which may be due to the W_2C 0002 reflection but is less strong than expected for randomly oriented W_2C. The GIXRD pattern for the layer with f_{CH4} = 1% exhibits the same three reflections from the W_2C phase but also a peak at $2\theta = 37.42 \pm 0.02°$. We note that this peak is approximately half-way between the reported peak positions of 36.9° for WC_y 111 [76] and 38.029° for W_2C 0002 (JCPDS 35-0776) such that this peak could be attributed to either of these two phases, as indicated in the figure by the triangle/square label. The GIXRD patterns from the layers with f_{CH4} = 2%, 4% and 6% show only one detectable layer peak each at 2θ = 36.74° to 36.72° to 36.49°, respectively. They are attributed to WC_y 111 reflections. Their position shifts to lower 2θ values starting from f_{CH4} =1% with 2θ = 37.42°, indicating an increasing lattice constant with increasing carbon content, consistent with the powder diffraction results and discussed in more detail below. The other reflections from cubic WC_y which are expected at 42.8, 62.0, 74.2 and 78.2° for 200, 220, 311and 222 reflections cannot be clearly seen in the GIXRD patterns but are present for powder scans. This is attributed to the relatively low peak-to-noise ratio in the GIXRD scans. The feature at ~29° for f_{CH4} = 2% is associated with a reflection from the sample

stage caused by the grazing incidence geometry of GIXRD scans. No corresponding peak is detected in powder scans. Grazing incidence x-ray diffraction analyses are also performed on all samples with d = 10 nm (not shown). However, no peak can be detected except a single weak W_2C $20\bar{2}1$ reflection for the lowest-C-content layer (f_{CH4} = 0.4%). In summary, both divergent-beam powder XRD and GIXRD analyses indicate that the d = 600 nm layers contain misoriented grains which have a hexagonal W_2C phase a low f_{CH4} and a cubic WC_y phase at higher f_{CH4}. In contrast, no misoriented grains or secondary phases can be detected for d = 10 nm layers except small inclusions of W_2C grains for f_{CH4} = 0.4%.

Figure 3 shows typical XRD reciprocal space maps from three WC_y(001)/MgO(001) layers with d = 10 nm and f_{CH4} = 0.4%, 1% and 6%. They show asymmetric 113 reflections using color-filled iso-intensity contours in a logarithmic scale and are plotted in a plane of the reciprocal space defined by $k_{||} = 2\sin\theta\,\sin(\omega\text{-}\theta)/\lambda$ and $k_{\perp} = 2\sin\theta\,\cos(\omega\text{-}\theta)/\lambda$ which are the in-plane and out-of-plane reciprocal lattice vectors along the [110] and [001] directions, respectively. The plot also includes a scale bar for the reciprocal length and arrows to indicate the experimental ω-2θ and ω scanning directions, which are rotated by 25.24° with respect to $k_{\perp}$ and $k_{||}$. In all three maps, the strongest (red) intensity is from the substrate MgO 113 reflection. It displays doublet or triplet peaks and/or broadening along the ω direction, indicating multiple-domain (poor quality) MgO substrates, which is common for commercial magnesium oxide single crystal substrates [57, 77]. Additionally, the elongation crossing the substrate peaks from top-left to bottom-right are resolution streaks associated with the electronic noise from the fully open line detector. The WC_y 113 reflection from the f_{CH4} = 0.4% film appears as vertically elongated light blue intensity above the substrate peak. The elongation is due to incomplete constructive and destructive interference due to the finite layer thickness and possibly also to single crystal WC_y mosaicity in the film growth direction [70]. It corresponds to a FWHM peak width in the growth direction of $\Delta k_{\perp}$ = 0.115 ± 0.005 nm^{-1}, yielding an out-of-plane XRD coherence length of $\xi_{\perp} = 1 / \Delta k_{\perp}$ = 8.7 ± 0.4 nm. This is in good agreement with the θ-2θ scan from the same sample for which $\Gamma_{2\theta}$ = 1.0 ± 0.1° yields $\xi_{\perp}$ = 9.5 ± 0.8 nm. The WC_y 113 peak is horizontally aligned with the substrate peak, such that $k_{||} = \sqrt{2}/a_{MgO}$ = 3.358 nm^{-1} where a_{MgO} = 0.4212 nm is the MgO lattice constant. This indicates fully-strained epitaxial growth with $(001)_{WC} \,||\, (001)_{MgO}$ and $[100]_{WC} \,||\, [100]_{MgO}$. The film peak is 0.088 nm^{-1} above the substrate peak, indicating a lattice constant that is 1.2% smaller in the growth direction than in the film plane. Thus, the f_{CH4} = 0.4% film is in state of in-plane tensile strain. In contrast, the WC_y 113 reflection from the f_{CH4} = 1% film is very close to the MgO 113 peak and replicates the triplet due to the multiple domains of the substrate. The elongated WC_y peak (green) along the most intense central peak of MgO (red) has a FWHM peak width $\Delta k_{\perp}$ = 0.09 ± 0.01 nm^{-1}. This yields a vertical coherence length $\xi_{\perp} = 1 / \Delta k_{\perp}$ = 11 ± 2 nm, which is consistent with the out-of-plane coherence length $\xi_{\perp}$ = 12 ± 9 nm determined from the symmetric θ-2θ scan. The fully-strained WC_y film is 0.02 nm^{-1} below the MgO peak, indicating a small in-plane compressive stress. The compressive stress is much more pronounced for the layer deposited with f_{CH4} = 6%. The WC_y 113 peak from this layer is 0.112 nm^{-1} below the substrate, indicating a 7 times larger strain than for f_{CH4} = 1%. Thus, increasing f_{CH4} from 0.4% to 1% to 6% leads to a transition from tensile to compressive stress and an increasing out-of-plane lattice constant $a_{\perp} = 3/k_{\perp}$ = 0.4161, 0.4222, 0.4279 nm, respectively, which is in good agreement with 0.4157, 0.424, 0.428 nm from the XRD θ-2θ scans.

Figure 4(a) is a plot of the out-of-plane lattice constant $a_{\perp}$ vs the C-to-W ratio x. It includes the values measured by XRD θ-2θ scans from Figs. 2(a,b) and reciprocal space maps from Fig. 3,

plotted as diamonds and crosses, respectively, for both d = 10 and 600 nm indicated by blue and pink symbols. We note that both measurement methods are insensitive to polycrystalline or amorphous microstructures and only detect $a_\perp$ from epitaxial WC_y, which represents the majority of the d = 10 nm layers but only a small portion of the total layers for d = 600 nm, as discussed in more detail below. The C-to-W ratio ranges from x = 0.57 – 1.25 and is determined by EDS analyses from 600-nm-thick layers as shown in Fig. 1. The data from the two sample sets as well as the two measurement methods are in good agreement, with deviations of only 0.2 – 0.6%. The lattice constant increases monotonically with increasing x, from $a_\perp$ = 0.4162 nm for $WC_{0.57}$ to $a_\perp$ = 0.422, 0.4275, 0.4275, and 0.4280 nm for $WC_{0.69}$, $WC_{0.89}$, $WC_{1.08}$, and $WC_{1.25}$. Here we use the plotted values from the RSM measurements on the d = 10 nm layers, because they have the smallest experimental uncertainty. The dotted horizontal line at a_{MgO} = 0.4212 nm indicates the lattice constant of the MgO substrate, which also corresponds to the in-plane lattice constants $a_\parallel$ of the epitaxial WC_y layers, since they are fully strained and coherent with the substrate. Thus, the transition from data points below to above the line indicates the transition from in-plane tension for x = 0.57 to in-plane compression for x = 0.69.

Figure 4(b) is a plot of the relaxed lattice constant a_o vs total carbon content x, measured from the epitaxial (green symbols) and polycrystalline (orange) portions of the 600-nm-thick WC_x layers. The plot includes the results from our density functional theory calculations. The measured lattice constant from the epitaxial WC_y, plotted as green symbols in Fig. 4(b), increases from 0.419 to 0.423, 0.423, 0.4243 and 0.426 nm with increasing x = 0.57, 0.69, 0.89, 1.08 to 1.25. It is determined using $a_o = (a_\perp - \nu a_\perp + 2\nu a_\parallel)/(1 + \nu)$ where $a_\perp$ is obtained from θ-2θ scans from 600-nm-thick films, $a_\parallel = a_{MgO}$ = 0.4212 nm, and ν = 0.29 is the calculated Poisson's ratio for cubic stoichiometric WC [78]. We note that a_o is relatively insensitive to the exact value of the chosen Poisson's ratio, as for example varying ν from 0.2 to 0.3 leads to only a 0.07% change in a_o. The solid orange data points at 0.4234, 0.4236 and 0.426 nm for x = 0.89, 1.08 and 1.25 are determined using the 111 reflection from the grazing incidence x-ray diffraction patterns shown in Fig. 2(e). That is, they represent the lattice constants from randomly oriented nanocrystalline rocksalt-structure grains in the d = 600 nm films. There is no orange data point plotted for the layer with x = 0.57, because no GIXRD signal from the cubic phase could be detected for this layer. Similarly, the pattern in Fig. 2(e) from the x = 0.69 layer indicates that a large fraction of this layer has crystallized in the W_2C phase and that the peak at 37.42° can be either due to the cubic WC_y or the hexagonal W_2C phase. Correspondingly, the orange data point (open triangle) at x = 0.69 in Fig. 4(b) indicates a lattice constant of 0.416 nm under the assumption that the questionable peak in Fig. 2(e) is from the cubic WC_y 111 reflection. However, the very low a_o makes this assumption unlikely, as also discussed in Section IV, suggesting that the polycrystalline carbide in the x = 0.69 layer exhibits the W_2C phase. In contrast, the datapoints for $x \geq 0.89$ are plotted as solid triangles, because the polycrystalline portion of these layers is phase-pure cubic WC_y. We note that there is good agreement between the green and orange data sets for $x \geq 0.89$, indicating that the epitaxial and randomly oriented portions of each layer have comparable lattice constants, suggesting that they also have comparable C-to-W ratios within their cubic WC_y phase, as discussed in more detail in section IV.

Fig. 4(b) also shows the lattice constants predicted by our first-principles calculations. The purple cross, circle, square and triangle shaped data points correspond to different C-vacancy arrangements in cubic WC_y, more specifically, vacancies on regular 3D sublattices, close-packed (111)-planes, (001)-planes, and close-packed [110]-lines, respectively, as described in section II. The calculated a_o values increase approximately linearly with x, as highlighted by the dashed line

which is obtained from a linear fit and corresponds to $a_o = (0.4053 + 0.0295 \times y)$ nm for cubic WC_y with $0.3 < y < 1.0$. Extrapolation to $y = 0$ yields a lattice constant $a_o = 0.4053$ nm for fcc W, which is approximately 1% above the previously reported calculated values of 0.39 [79] and 0.40 nm [80, 81], but 2.3% below the experimental 0.415 nm from selected area electron diffraction patterns of sputter deposited fcc W [82]. Our measured lattice constants are below the purple line. This suggests that the cubic WC_y in our layers have more C-vacancies than expected based on the measured W-to-C ratio x, as discussed quantitatively in section IV.

Figure 5 shows cross-sectional transmission electron micrographs from a 600-nm-thick WC_x layer deposited with $f_{CH4} = 6\%$. The micrograph in Fig. 5(a) is obtained along the 100 zone axis using a 10 μm objective aperture to enhance diffraction contrast by excluding most diffracted electrons from the image. The MgO substrate appears relatively bright at the bottom of the micrograph. The WC layer is considerably darker, due to the high atomic mass of tungsten. It is slightly brighter near the top of the micrograph, which is due to a decreasing specimen thickness. The bottom 12 nm of the WC layer exhibits a nearly uniform contrast and is particularly dark, and represents the epitaxial portion of the layer. Above this region, the micrograph exhibits features that are elongated along the growth direction and are separated by lower-density boundaries, indicating a columnar growth mode with an average 7 nm column width. In addition, intracolumnar contrast variations with characteristic distances of 2 - 10 nm in the vertical direction indicate a nanocrystalline microstructure with an estimated grain size of 2 - 10 nm. This is in agreement with the 8 nm determined from the peak width of the 111 reflection in the grazing incidence XRD pattern shown in Fig. 2(e) from the same sample. We note, however, that grain boundaries are not clearly defined in this micrograph and high-resolution micrographs (not shown) exhibit crystalline regions as well as more random atomic arrangements, which indicate considerable crystalline disorder, multiple grain orientations within the specimen depth and/or amorphous regions. The inset in Fig. 5(a) is a selected area diffraction pattern (SADP) obtained using a selected area aperture centered ~300 nm above the layer-substrate interface such that the diffracted intensity originates primarily from the nanocrystalline WC_y and may include some epitaxial film region but excludes the MgO(001) substrate. The pattern exhibits rings at 4.1, 4.6, 6.67 and 7.82 nm^{-1} which are attributed to WC_y 111, 200, 220, and 311 reflections as labeled. We note that the accuracy in the measured radii of the 111 and 200 rings is limited because the intensity of these two rings overlap. They cannot be clearly separated because the high atomic mass of W requires converging the electron beam in order to obtain sufficient intensity during the diffraction experiments. In contrast, the 220 and 311 diffraction rings are quite clear and yield a lattice constant of $a_o = 0.424 \pm 0.003$ nm, in good agreement with $a_o = 0.425$ nm from the XRD measurements.

Figure 5(b) is a high resolution TEM micrograph of the substrate-layer interface from the same sample. It is obtained with a many-beam geometry along the 100 zone axis using a 100-μm objective aperture. Lattice fringes in both the horizontal and vertical directions are clearly visible. They correspond to 020 and 002 planes and are continuous across the interface from the MgO(001) substrate at the bottom and the WC_y(001) layer at the top of the micrograph. This indicates a cube-on-cube epitaxial WC_y film growth with $(001)_{WC} \parallel (001)_{MgO}$ and $[100]_{WC} \parallel [100]_{MgO}$ for the initial approximately 12 nm, confirming the XRD results. The interface between the epitaxial WC_y(001) and the MgO(001) substrate is indicated by the vertical contrast variation near the middle of the micrograph, which is due to the atomic mass difference between the WC_y film and the MgO substrate. The horizontal contrast variations are attributed to local strain variations, non-uniform film thickness and/or atoms redeposited on the specimen surface during sample

preparation. The vertical contrast at the WC/MgO interface occurs over approximately three monolayers, suggesting that the MgO surface is not atomically flat but exhibits atomic steps, similar to what has been reported for the Cu/MgO interface [83].

Inverse Fast Fourier Transform (FFT) analyses show the presence of misfit dislocations near the interface with an average spacing of 50 ± 10 nm. The lattice mismatch between this layer and the substrate is $\delta = a_o/a_{MgO}$ -1 = 0.4255/0.4212-1 = 1.0%, yielding a theoretical spacing of misfit dislocations for a fully relaxed layer of $a_o/2\delta$ = 21 ± 1 nm. Thus, this film is partially relaxed after TEM sample preparation with the degree of relaxation $R = (a_{\parallel} - a_{MgO})/(a_o - a_{MgO})$ = 42 ± 12%. This is in direct contrast to the reciprocal space mapping from the same sample in Fig. 3, which show that the as-deposited layer is fully strained with an estimated upper bound for R of 15%. Correspondingly, we attribute the stain relaxation to TEM sample preparation. More specifically, FIB induced defects could facilitate relaxation [84, 85] and/or the two new free surfaces of the electron transparent lamella allow easy nucleation and glide of misfit dislocations [86]. The inset in Fig. 5(b) is the SADP obtained using a selected area aperture centered at the WC_y-MgO interface. It shows a single crystal diffraction pattern as expected from the rock-salt structure MgO. No secondary pattern from the epitaxial WC_y can be detected, which is attributed to the close proximity of the expected diffraction spots from the substrate and layer, as the out-of-plane lattice constant of this layer is only 1.9% larger than for MgO, based on our XRD RSM shown in Fig. 3 and this difference becomes even smaller as the layer is partially relaxed. In addition, the limited 10 nm thickness of the epitaxial WC_y in combination with the beam attenuation in high-atomic-mass WC_y is expected to yield only weak diffraction spots from the layer. This SADP in Fig. 5(b) also shows a weak ring from diffracted intensity of the polycrystalline portion of the WC_x layer.

IV. Discussion

In this section, we first discuss the microstructure of the deposited WC_x layers, including the transition from fully strained epitaxial layers to a polycrystalline microstructure, and then discuss the composition dependence of the lattice constant of cubic WC_y from both XRD measurements and first principles calculations. The first evidence for an epitaxial breakdown in our WC_x/MgO(001) layers is obtained from XRD θ-2θ scans in Figs. 2(a) and (b): They show the same WC_y 002 peak widths and intensities for d = 10 and 600 nm, suggesting that the 10- and 600-nm-thick films contain approximately the same amount of epitaxial WC_y(001). The epitaxy of this cubic WC_y phase is confirmed by the narrow rocking curves (0.04-0.12°) for all layers, the reciprocal space maps, and the high-resolution TEM analysis including the associated electron diffraction pattern. GIXRD 2θ scans from 600-nm-thick layers reveal 111, 200, 220, 311, 222 reflections from cubic WC_y as well as peaks from W_2C for layers with low carbon content, but no GIXRD peaks can be detected for d = 10 nm layers. This indicates that d = 600 nm layers contain a polycrystalline microstructure, but no evidence for misoriented grains can be detected for d = 10 nm. These overall results suggest that the deposited WC_x first forms an approximately 10-nm-thick epitaxial WC_y(001) layer, followed by a polycrystalline carbide. The thickness of 10 nm is in excellent agreement with the TEM micrograph in Fig. 5(a) which shows an approximately 12-nm-thick dark contrast at the bottom of the deposited layer. It is also in agreement with the measured out-of-plane XRD coherence length in Fig. 2(c) which ranges from 8-14 nm. The epitaxial WC_y(001) is fully strained and coherent with the MgO(001) substrate, as determined by the RSMs shown in Fig. 3. We attribute the transition from an epitaxial to a polycrystalline microstructure after ~10 nm of growth to an epitaxial breakdown. The exact reasons for this breakdown are not known, but may be related to kinetic surface roughening and epitaxial strain fields that cause

carbon atoms to segregate along pits of rough surfaces, forming nucleation sites for randomly oriented grains that result in the epitaxial breakdown. Some evidence for this postulated mechanism is the relatively large root-mean-square surface roughness of 1.0-1.5 nm measured by XRR for the d = 10 nm layers. Continued film growth in combination with carbon segregation to grain boundaries and the top surface leads to frequent carbide grain renucleation and the formation of a nanocrystalline microstructure with grain sizes of 2-10 nm, as observed in Fig. 5(a). Similar epitaxial breakdown mechanisms have been reported for Si [87] and GaAs [88]. We note that the out-of-plane coherence length is largest for f_{CH4} = 1%, as shown in Fig. 2(d). This layer has the smallest lattice mismatch with the substrate and correspondingly the smallest strain, suggesting that the epitaxial breakdown is directly or indirectly facilitated or enhanced by strain.

We focus now our discussion on the composition dependence of the lattice constant of cubic WC_y. The results from our first principles calculations plotted in Fig. 4(b) indicate an approximately linear increase in the lattice constant a_o = (0.4053 + 0.0295y) nm for rocksalt structure WC_y where the deviation from stoichiometry (y < 1) is caused by C vacancies. Our measured values from the epitaxial region in the 600-nm-thick films plotted as green data points in Fig. 4(b) also increase with carbon content. However, the increase is non-linear and the experimental lattice constants are below the calculated values. More specifically, the measured a_o increases steeply for x = 0.57 - 0.69 and then more moderately for x > 0.69. We note that the corresponding measured a_o from the 10-nm-thick layers shows a similar non-linear composition dependence with steep and moderate increases for x = 0.57 - 0.69 and x = 0.69 – 0.89, respectively, and a nearly constant a_o for x = 0.89 – 1.25. The two measured a_o data sets from the epitaxial portions of the 10 and 600-nm-thick layers agree within experimental uncertainty, as evident from the plotted $a_\perp$ in Fig. 4(a), such that only the latter set is used in the following discussion. The initial steep slope from x = 0.57 - 0.69 matches the slope from our simulations and the measured a_o is just 0.7% below the predictions for both x = 0.57 and 0.69. This deviation can be accounted for by the uncertainty in the DFT calculations, which are done with the revised Perdew-Burke-Ernzerhof generalized gradient approximation PBEsol, which has been reported to yield accurate lattice constants for densely packed solids with a mean error of 0.0029 nm [61], corresponding to an estimated 0.7% uncertainty for cubic tungsten carbide. However, the deviation between experiment and simulations grows to 2%, 3% and 4% for x = 0.89, 1.08 and 1.25, which is well above the uncertainty that can be attributed to the DFT calculations. We attribute this disagreement to a fraction of C atoms not incorporating into the cubic WC_y phase but to segregate and form graphitic and/or amorphous carbon a-C:H which may contain hydrogen because the C-source during deposition is methane. This amorphous C phase may also contribute to the epitaxial breakdown discussed above. We note that W vacancies in cubic WC_y could, in principle, explain the suppression of the lattice constant at large x > 1.0. However, as described in Section II, they are energetically unfavorable and are therefore expected to be negligible. We also note that our measured values are in good agreement with previous experimental studies with reported a_o = 0.422 nm for $WC_{0.61}$ [89], 0.4215 nm for $WC_{0.82}$ [47], 0.4252 nm and 0.4266 nm for nominal $WC_{0.85}$ and $WC_{1.00}$ [90].

Table I lists the measured C-to-W ratio x in our 600-nm-thick WC_x layers as a function of f_{CH4}. It also lists the C-to-W ratio y in the cubic WC_y phase within the layers. Note, the subscripts x and y refer to the total C content within the layer and the C content within the cubic phase, respectively, as introduced before and consistently used throughout the paper. The listed x ranges from 0.57 to 1.25 and is directly obtained from our EDS and RBS/EBS analyses presented in Fig. 1. The listed y = 0.47 – 0.68 is determined from the measured lattice constant and assuming that

the linear prediction from the DFT calculations is correct. Thus, $y = (a_o - 0.4053)/0.0295$, where a_o is the measured lattice constant for a specific sample deposited with f_{CH4}. The carbon content in the cubic phase increases with increasing total carbon content. However, the table suggests that y saturates at ~0.7±0.1, indicating that cubic WC_y is most stable with a considerable fraction of C vacancies. This is in excellent agreement with our DFT predictions of a negative C vacancy formation energy described in Section II. This argument is also consistent with what has been proposed by Toth [1], describing cubic WC_y as close-packed (fcc) W containing carbon atoms on interstitial sites which cause increasing lattice distortions with increasing y, ultimately destabilizing the cubic phase for large y. We note that the lattice constants measured by GIXRD for the cubic WC_y in the nanocrystalline structure plotted as solid orange triangles in Fig. 4(b) are in good agreement with the epitaxial values, suggesting that the nanocrystalline upper part of the deposited layers exhibit a comparable y as the epitaxial lower part. This agreement is experimentally valid for $x \geq 0.89$ where the polycrystalline structure consists of cubic WC_y. In contrast, no direct conclusion can be drawn for the layers with low carbon content ($x \leq 0.69$) since the lattice constants of their nanocrystalline hexagonal W_2C grains cannot be directly compared with their cubic epitaxial part. The transition from cubic WC_y to hexagonal W_2C with decreasing x is consistent with the previously reported W-C phase diagram [46] which indicates a lower boundary of the homogeneity range for cubic tungsten carbide at $x = 0.59$.

Table I also includes the volume fraction of amorphous carbon a-C:H in the 600-nm-thick WC_x layers, as estimated from the layer thickness d measured by SEM, the total W areal density ρ_W measured by RBS, and the C-to-W ratios x and y. This is done most directly for the two layers with $f_{CH4} = 2\%$ and 6% for which ρ_W is measured by RBS, such that the effective carbide thickness $d_{WC} = \rho_W a_o^3/4 = 620$ and 490 nm, respectively, where the lattice constant a_o is obtained from XRD measurements for each sample and the division by 4 is due to the conventional cubic WC_y unit cell containing 4 W atoms. Correspondingly, the volume fraction for the carbide $\%V_{WC} = d_{WC} / d = 87 \pm 8\%$ and $74 \pm 11\%$ for the layers with $x = 0.89$ and 1.25, respectively, and the volume fraction of amorphous carbon $\%V_{a\text{-}C} = 1 - \%V_{WC} = 13 \pm 8\%$ and $26 \pm 11\%$, as listed in Table I and labeled with "*". Using this $\%V_{a\text{-}C}$, as well as d and the listed x and y, we determine a density for the a-C:H of $\rho_{a\text{-}C} = 2.0$ and 1.7 g/cm^3 for $x = 0.89$ and 1.25, respectively, neglecting the mass of hydrogen. These values are slightly larger than the reported density range of 1.2 – 1.6 g/cm^3 for plasma deposited soft a-C:H from Ref. [91] and references therein, while the overall reported density range for a-C:H with varying sp^2/sp^3 bonding is 0.95 - 3.5 g/cm^3 [92]. We note that the 8-11% uncertainty in $\%V_{a\text{-}C}$ causes a large uncertainty in the estimated a-C:H density such that any $\rho_{a\text{-}C}$ within 0.8 – 3.8 g/cm^3 would be consistent with our measurements. This uncertainty-range is even slightly larger than the range of any realistic a-C:H density.

Secondly, we determine the volume fraction of a-C:H for the layer with $f_{CH4} = 4\%$, using $\%V_{a\text{-}C} = \tilde{V}_{a\text{-}C}/[\tilde{V}_{a\text{-}C} + \tilde{V}_{WC}/(x\text{-}y)]$, where $\tilde{V}_{WC}$ and $\tilde{V}_{a\text{-}C}$ are the molar volumes of WC_y and a-C:H, respectively. $\tilde{V}_{WC} = N_A \times a_o^3/4 = 11.50$ cm^3/mol is directly determined from Avogadro's number N_A and the measured $a_o = 0.4243$ nm, while $\tilde{V}_{a\text{-}C} = 6.0$ cm^3/mol is estimated assuming $\rho_{a\text{-}C} = 2$ g/cm^3 and neglecting the mass of hydrogen. This yields $\%V_{a\text{-}C} = 19\%$ for the layer with $f_{CH4} = 4\%$, as listed in Table I. We use the same approach to determine $\%V_{a\text{-}C}$ for $f_{CH4} = 2\%$ and 6% and include the resulting values also in Table I, labeled with "†". Thirdly, $\%V_{a\text{-}C}$ is obtained for the layers with $f_{CH4} = 0.4\%$ and 1% which exhibit primarily the hexagonal W_2C phase. Thus, the measured y from the epitaxial cubic part cannot be directly used to determine the C distribution in the polycrystalline part. Instead we assume a stoichiometric W_2C carbide phase and use $\%V_{a\text{-}C} = \tilde{V}_{a\text{-}C}/[\tilde{V}_{a\text{-}C} + \tilde{V}_{W2C}/(x\text{-}0.5)]$ where $\tilde{V}_{a\text{-}C} = 6.0$ cm^3/mol from above and $\tilde{V}_{W2C} = 10.8$ and 11.3 cm^3/mol

from the measured lattice constants c and a of the hexagonal W_2C phase from Fig. 2(e) for the f_{CH4} = 0.4% and 1% films, respectively. This yields $\%V_{a\text{-}C}$ = 4 and 9 % for f_{CH4} = 0.4% and 1%, as labeled with "#" in Table 1. In summary, the volume fraction of amorphous C increases from 4% to 26% with increasing C content x = 0.57-1.25.

V. Conclusions

10-nm-thick epitaxial rock-salt structure WC_y(001) films deposited on MgO(001) by reactive magnetron sputtering in Ar/CH_4 gas mixtures at 400 °C are fully strained and exhibit a cube-on-cube epitaxial relationship with $(001)_{WC} \parallel (001)_{MgO}$ and $[100]_{WC} \parallel [100]_{MgO}$, as confirmed by x-ray diffraction and transmission electron microscopy analyses. Continued growth of WC_x layers above d = 10 nm leads to an epitaxial breakdown and the nucleation of misoriented grains for $x \geq 0.89$ and a secondary W_2C phase for $x \leq 0.69$. This transition to a nanocrystalline microstructure is attributed to carbon segregation in combination with epitaxial strain fields and surface roughening. Evidence for C segregation is obtained from the measured relaxed lattice constant of cubic WC_y, which increases from a_o = 0.419 to 0.425 nm with an increasing measured C-to-W ratio x = 0.57 - 1.25. This measured a_o is well below our DFT predictions of a_o = (0.4053 + 0.0295 y) nm for cubic WC_y, suggesting that the carbon vacancy density is larger than the measured x suggests. This is consistent with the negative calculated vacancy formation energy and indicates that the tungsten carbide rock-salt structure is stabilized by C vacancies. As a consequence, only a fraction of the deposited carbon incorporates into the carbide phase while the remainder likely forms a-C:H between carbide nanocrystals with an a-C:H volume fraction increasing from 4% for x = 0.59 to 26% for x = 1.25.

Acknowledgements

The authors acknowledge financial support by the National Science Foundation under Grant Nos. 1712752, 1629230 and 1629239.

References

[1] L.E. Toth, Transition metal carbides and nitrides, Academic Press, 1971.
[2] J. Musil, Hard and superhard nanocomposite coatings, Surface and Coatings Technology, 125 (2000) 322-330.
[3] S. Niyomsoan, W. Grant, D.L. Olson, B. Mishra, Variation of color in titanium and zirconium nitride decorative thin films, Thin Solid Films, 415 (2002) 187-194.
[4] M. Wittmer, TiN and TaN as diffusion barriers in metallizations to silicon semiconductor devices, Applied Physics Letters, 36 (1980) 456-458.
[5] Y. Zhong, X. Xia, F. Shi, J. Zhan, J. Tu, H.J. Fan, Transition Metal Carbides and Nitrides in Energy Storage and Conversion, Advanced Science, 3 (2016) 1500286.
[6] B. Gao, X. Li, K. Ding, C. Huang, Q. Li, P. K. Chu, K. Huo, Recent progress in nanostructured transition metal nitrides for advanced electrochemical energy storage, Journal of Materials Chemistry A, 7 (2019) 14-37.
[7] W.-F. Chen, J.T. Muckerman, E. Fujita, Recent developments in transition metal carbides and nitrides as hydrogen evolution electrocatalysts, Chemical Communications, 49 (2013) 8896-8909.
[8] N. Nedfors, O. Tengstrand, E. Lewin, A. Furlan, P. Eklund, L. Hultman, U. Jansson, Structural, mechanical and electrical-contact properties of nanocrystalline-NbC/amorphous-C coatings deposited by magnetron sputtering, Surface and Coatings Technology, 206 (2011) 354-359.
[9] K. Nygren, M. Samuelsson, A. Flink, H. Ljungcrantz, Å. Kassman Rudolphi, U. Jansson, Growth and characterization of chromium carbide films deposited by high rate reactive magnetron sputtering for electrical contact applications, Surface and Coatings Technology, 260 (2014) 326-334.
[10] N. Szymanski, I. Khatri, J. Amar, D. Gall, S. Khare, Unconventional superconductivity in 3d rocksalt transition metal carbides, Journal of Materials Chemistry C, 7 (2019) 12619-12632.

[11] T. Vitu, T. Polcar, L. Cvrcek, R. Novak, J. Macak, J. Vyskocil, A. Cavaleiro, Structure and tribology of biocompatible Ti–C:H coatings, Surface and Coatings Technology, 202 (2008) 5790-5793.
[12] H. Wang, S. Zhang, Y. Li, D. Sun, Bias effect on microstructure and mechanical properties of magnetron sputtered nanocrystalline titanium carbide thin films, Thin Solid Films, 516 (2008) 5419-5423.
[13] C. Metaxa, S. Kassavetis, J.F. Pierson, D. Gall, P. Patsalas, Infrared Plasmonics with Conductive Ternary Nitrides, ACS Applied Materials & Interfaces, 9 (2017) 10825-10834.
[14] P. Patsalas, C. Charitidis, S. Logothetidis, The effect of substrate temperature and biasing on the mechanical properties and structure of sputtered titanium nitride thin films, Surface and Coatings Technology, 125 (2000) 335-340.
[15] J.-E. Sundgren, B.-O. Johansson, S.-E. Karlsson, H.T.G. Hentzell, Mechanisms of reactive sputtering of titanium nitride and titanium carbide II: Morphology and structure, Thin Solid Films, 105 (1983) 367-384.
[16] A.A. Koverga, E. Flórez, L. Dorkis, J.A. Rodriguez, CO, CO_2 , and H_2 Interactions with (0001) and (001) Tungsten Carbide Surfaces: Importance of Carbon and Metal Sites, The Journal of Physical Chemistry C, 123 (2019) 8871-8883.
[17] B. Wei, G. Tang, H. Liang, Z. Qi, D. Zhang, W. Hu, H. Shen, Z. Wang, Bimetallic vanadium-molybdenum nitrides using magnetron co-sputtering as alkaline hydrogen evolution catalyst, Electrochemistry Communications, 93 (2018) 166-170.
[18] A. Achour, R.L. Porto, M.-A. Soussou, M. Islam, M. Boujtita, K.A. Aissa, L. Le Brizoual, A. Djouadi, T. Brousse, Titanium nitride films for micro-supercapacitors: Effect of surface chemistry and film morphology on the capacitance, Journal of Power Sources, 300 (2015) 525-532.
[19] A.P. Ehiasarian, P.E. Hovsepian, L. Hultman, U. Helmersson, Comparison of microstructure and mechanical properties of chromium nitride-based coatings deposited by high power impulse magnetron sputtering and by the combined steered cathodic arc/unbalanced magnetron technique, Thin Solid Films, 457 (2004) 270-277.
[20] D. Gall, I. Petrov, N. Hellgren, L. Hultman, J.E. Sundgren, J.E. Greene, Growth of poly- and single-crystal ScN on MgO(001): Role of low-energy N_2^+ irradiation in determining texture, microstructure evolution, and mechanical properties, Journal of Applied Physics, 84 (1998) 6034-6041.
[21] C.-S. Shin, D. Gall, N. Hellgren, J. Patscheider, I. Petrov, J.E. Greene, Vacancy hardening in single-crystal TiN_x(001) layers, Journal of Applied Physics, 93 (2003) 6025-6028.
[22] J.S. Chawla, X.Y. Zhang, D. Gall, Effective electron mean free path in TiN(001), Journal of Applied Physics, 113 (2013) 063704.
[23] A. B. Mei, M. Tuteja, D. G. Sangiovanni, R. T. Haasch, A. Rockett, L. Hultman, I. Petrov, J. E. Greene, Growth, nanostructure, and optical properties of epitaxial VN_x /MgO(001) ($0.80 \leqslant x \leqslant 1.00$) layers deposited by reactive magnetron sputtering, Journal of Materials Chemistry C, 4 (2016) 7924-7938.
[24] D. Gall, C.-S. Shin, T. Spila, M. Odén, M.J.H. Senna, J.E. Greene, I. Petrov, Growth of single-crystal CrN on MgO(001): Effects of low-energy ion-irradiation on surface morphological evolution and physical properties, Journal of Applied Physics, 91 (2002) 3589-3597.
[25] X.Y. Zhang, J.S. Chawla, B.M. Howe, D. Gall, Variable-range hopping conduction in epitaxial CrN(001), Physical Review B, 83 (2011) 165205.
[26] M.E. McGahay, D. Gall, Conductive surface oxide on CrN(001) layers, Applied Physics Letters, 114 (2019) 131602.
[27] K. Zhang, K. Balasubramanian, B.D. Ozsdolay, C.P. Mulligan, S.V. Khare, W.T. Zheng, D. Gall, Growth and mechanical properties of epitaxial NbN(001) films on MgO(001), Surface and Coatings Technology, 288 (2016) 105-114.
[28] B.D. Ozsdolay, K. Balasubramanian, D. Gall, Cation and anion vacancies in cubic molybdenum nitride, Journal of Alloys and Compounds, 705 (2017) 631-637.
[29] H.-S. Seo, T.-Y. Lee, J.G. Wen, I. Petrov, J.E. Greene, D. Gall, Growth and physical properties of epitaxial HfN layers on MgO(001), Journal of Applied Physics, 96 (2004) 878-884.
[30] C.-S. Shin, Y.-W. Kim, D. Gall, J.E. Greene, I. Petrov, Phase composition and microstructure of polycrystalline and epitaxial TaN*x* layers grown on oxidized Si(001) and MgO(001) by reactive magnetron sputter deposition, Thin Solid Films, 402 (2002) 172-182.
[31] B.D. Ozsdolay, C.P. Mulligan, M. Guerette, L. Huang, D. Gall, Epitaxial growth and properties of cubic WN on MgO(001), MgO(111), and Al_2O_3(0001), Thin Solid Films, 590 (2015) 276-283.
[32] M. Braic, N.C. Zoita, M. Danila, C.E.A. Grigorescu, C. Logofatu, Hetero-epitaxial growth of TiC films on MgO(001) at 100°C by DC reactive magnetron sputtering, Thin Solid Films, 589 (2015) 590-596.
[33] J. Carroll, R. Krchnavek, C. Lunk, T. Scabarozi, S. Lofland, J. Hettinger, An investigation of the properties of epitaxial chromium-substituted vanadium carbide thin films, Vacuum, 109 (2014) 212-215.

[34] K. Zhang, K. Balasubramanian, B. Ozsdolay, C. Mulligan, S. Khare, W. Zheng, D. Gall, Epitaxial NbC_xN_{1-x} (001) layers: Growth, mechanical properties, and electrical resistivity, Surface and Coatings Technology, 277 (2015) 136-143.
[35] H. Zaid, A. Aleman, K. Tanaka, C. Li, P. Berger, T. Back, J. Fankhauser, M.S. Goorsky, S. Kodambaka, Influence of ultra-low ethylene partial pressure on microstructural and compositional evolution of sputter-deposited Zr-C thin films, Surface and Coatings Technology, 398 (2020).
[36] S. Kacim, L. Binst, F. Reniers, F. Bouillon, Composition and structure of reactively sputter-deposited molybdenum-carbon films, Thin Solid Films, 287 (1996) 25-31.
[37] U. Jansson, H. Högberg, J.-P. Palmqvist, L. Norin, J.O. Malm, L. Hultman, J. Birch, Low temperature epitaxial growth of metal carbides using fullerenes, Surface and Coatings Technology, 142-144 (2001) 817-822.
[38] P. Eklund, J. Rosen, P.O.Å. Persson, Layered ternary $M_{n+1}AX_n$ phases and their 2D derivative MXene: an overview from a thin-film perspective, Journal of Physics D: Applied Physics, 50 (2017) 113001.
[39] A.S. Ingason, A. Petruhins, J. Rosen, Toward structural optimization of MAX phases as epitaxial thin films, Materials Research Letters, 4 (2016) 152-160.
[40] S.X. Du, M. Wen, P. Ren, Q.N. Meng, K. Zhang, W.T. Zheng, Deposition and Characterization of Reactive Magnetron Sputtered Tungsten Carbide Films, Materials Science Forum; Pfaffikon, 898 (2017) 1505-1511.
[41] K. Abdelouahdi, C. Sant, C. Legrand-Buscema, P. Aubert, J. Perrière, G. Renou, P. Houdy, Microstructural and mechanical investigations of tungsten carbide films deposited by reactive RF sputtering, Surface and Coatings Technology, 200 (2006) 6469-6473.
[42] M.D. Abad, M.A. Muñoz-Márquez, S. El Mrabet, A. Justo, J.C. Sánchez-López, Tailored synthesis of nanostructured WC/a-C coatings by dual magnetron sputtering, Surface and Coatings Technology, 204 (2010) 3490-3500.
[43] R.B. Levy, M. Boudart, Platinum-Like Behavior of Tungsten Carbide in Surface Catalysis, Science, 181 (1973) 547-549.
[44] M.C. Weidman, D.V. Esposito, I.J. Hsu, J.G. Chen, Electrochemical Stability of Tungsten and Tungsten Monocarbide (WC) Over Wide pH and Potential Ranges, Journal of The Electrochemical Society, 157 (2010) F179-F188.
[45] S. Emin, C. Altinkaya, A. Semerci, H. Okuyucu, A. Yildiz, P. Stefanov, Tungsten carbide electrocatalysts prepared from metallic tungsten nanoparticles for efficient hydrogen evolution, Applied Catalysis B: Environmental, 236 (2018) 147-153.
[46] A.S. Kurlov, A.I. Gusev, Phase equilibria in the W–C system and tungsten carbides, Russian Chemical Reviews, 75 (2006) 617-636.
[47] R.V. Sara, Phase Equilibria in the System Tungsten—Carbon, Journal of the American Ceramic Society, 48 (1965) 251-257.
[48] D.V. Suetin, I.R. Shein, A.L. Ivanovskii, Structural, electronic properties and stability of tungsten mono- and semi-carbides: A first principles investigation, Journal of Physics and Chemistry of Solids, 70 (2009) 64-71.
[49] A.S. Kurlov, A.I. Gusev, Tungsten carbides and W-C phase diagram, Inorganic Materials, 42 (2006) 121-127.
[50] C. Rincón, J. Romero, J. Esteve, E. Martínez, A. Lousa, Effects of carbon incorporation in tungsten carbide films deposited by r.f. magnetron sputtering: single layers and multilayers, Surface and Coatings Technology, 163-164 (2003) 386-391.
[51] J. Nazon, M. Herbst, M.C. Marco de Lucas, S. Bourgeois, B. Domenichini, WC-based thin films obtained by reactive radio-frequency magnetron sputtering using W target and methane gas, Thin Solid Films, 591 (2015) 119-125.
[52] M.D. Abad, J.C. Sánchez-López, N. Cusnir, R. Sanjines, WC/a-C nanocomposite thin films: Optical and electrical properties, Journal of Applied Physics, 105 (2009) 033510.
[53] M. Katoh, H. Kawarada, Heteroepitaxial Growth of Tungsten Carbide Films on W(110) by Plasma-Enhanced Chemical Vapor Deposition, Japanese Journal of Applied Physics, 34 (1995) 3628-3630.
[54] J.-P. Palmquist, Z. Czigány, L. Hultman, U. Jansson, Epitaxial growth of tungsten carbide films using C_{60} as carbon precursor, Journal of Crystal Growth, 259 (2003) 12-17.
[55] L. Knoll, V. Teodorescu, R.A. Minamisawa, Ultra-Thin Epitaxial Tungsten Carbide Schottky Contacts in 4H-SiC, IEEE Electron Device Letters, 37 (2016) 1318-1320.
[56] U. Jansson, E. Lewin, Sputter deposition of transition-metal carbide films — A critical review from a chemical perspective, Thin Solid Films, 536 (2013) 1-24.
[57] B. Wang, D. Gall, Fully strained epitaxial $Ti_{1-x}Mg_xN$(001) layers, Thin Solid Films, (2019).
[58] E. Milosevic, S. Kerdsongpanya, A. Zangiabadi, K. Barmak, K.R. Coffey, D. Gall, Resistivity size effect in epitaxial Ru(0001) layers, Journal of Applied Physics, 124 (2018) 165105.

[59] P. Revesz, J. Li, G. Vizkelethy, J.W. Mayer, L.J. Matienzo, F. Emmi, 12C(α, α) 12C resonance as a tool for quantitative analysis, Nuclear Instruments and Methods in Physics Research Section B: Beam Interactions with Materials and Atoms, 58 (1991) 132-135.
[60] M. Mayer, Improved physics in SIMNRA 7, Nuclear Instruments and Methods in Physics Research Section B: Beam Interactions with Materials and Atoms, 332 (2014) 176-180.
[61] J.P. Perdew, A. Ruzsinszky, G.I. Csonka, O.A. Vydrov, G.E. Scuseria, L.A. Constantin, X. Zhou, K. Burke, Restoring the Density-Gradient Expansion for Exchange in Solids and Surfaces, Physical Review Letters, 100 (2008) 136406.
[62] G. Kresse, D. Joubert, From ultrasoft pseudopotentials to the projector augmented-wave method, Physical review b, 59 (1999) 1758.
[63] K. Balasubramanian, S. Khare, D. Gall, Vacancy-induced mechanical stabilization of cubic tungsten nitride, Physical Review B, 94 (2016) 174111.
[64] K. Balasubramanian, S.V. Khare, D. Gall, Energetics of point defects in rocksalt structure transition metal nitrides: Thermodynamic reasons for deviations from stoichiometry, Acta Materialia, 159 (2018) 77-88.
[65] B.D. Ozsdolay, C.P. Mulligan, K. Balasubramanian, L. Huang, S.V. Khare, D. Gall, Cubic β -WN x layers: Growth and properties vs N-to-W ratio, Surface and Coatings Technology, 304 (2016) 98-107.
[66] K. Balasubramanian, L. Huang, D. Gall, Phase stability and mechanical properties of $Mo_{1-x}N_x$ with $0 \leqslant x \leqslant 1$, Journal of Applied Physics, 122 (2017) 195101.
[67] E. Milosevic, P. Zheng, D. Gall, Electron Scattering at Epitaxial Ni(001) Surfaces, IEEE Transactions on Electron Devices, 66 (2019) 4326-4330.
[68] J.S. Chawla, D. Gall, Specular electron scattering at single-crystal Cu(001) surfaces, Applied Physics Letters, 94 (2009).
[69] J.M. Purswani, T. Spila, D. Gall, Growth of epitaxial Cu on MgO(001) by magnetron sputter deposition, Thin Solid Films, 515 (2006) 1166-1170.
[70] P. Zheng, B.D. Ozsdolay, D. Gall, Epitaxial growth of tungsten layers on MgO(001), Journal of Vacuum Science & Technology A: Vacuum, Surfaces, and Films, 33 (2015) 061505.
[71] J.S. Chawla, D. Gall, Epitaxial Ag(001) grown on MgO(001) and TiN(001): Twinning, surface morphology, and electron surface scattering, Journal of Applied Physics, 111 (2012).
[72] C.-S. Shin, D. Gall, P. Desjardins, A. Vailionis, H. Kim, I. Petrov, J. Greene, M. Odén, Growth and physical properties of epitaxial metastable cubic TaN (001), Applied Physics Letters, 75 (1999) 3808-3810.
[73] M.E. McGahay, B. Wang, J. Shi, D. Gall, Band gap and electron transport in epitaxial cubic $Cr_{1-x}Al_xN$(001), Physical Review B, 101 (2020).
[74] B. Wang, S. Kerdsongpanya, M.E. McGahay, E. Milosevic, P. Patsalas, D. Gall, Growth and properties of epitaxial $Ti_{1-x}Mg_xN$(001) layers, Journal of Vacuum Science & Technology A, 36 (2018) 061501.
[75] R. Deng, P.Y. Zheng, D. Gall, Optical and electron transport properties of rock-salt $Sc_{1-x}Al_xN$, Journal of Applied Physics, 118 (2015) 015706.
[76] A.-R. Ko, Y.-W. Lee, J.-S. Moon, S.-B. Han, G. Cao, K.-W. Park, Ordered mesoporous tungsten carbide nanoplates as non-Pt catalysts for oxygen reduction reaction, Applied Catalysis A: General, 477 (2014) 102-108.
[77] J.L. Schroeder, A.S. Ingason, J. Rosén, J. Birch, Beware of poor-quality MgO substrates: A study of MgO substrate quality and its effect on thin film quality, Journal of Crystal Growth, 420 (2015) 22-31.
[78] K. Balasubramanian, S.V. Khare, D. Gall, Valence electron concentration as an indicator for mechanical properties in rocksalt structure nitrides, carbides and carbonitrides, Acta Materialia, 152 (2018) 175-185.
[79] H.J.F. Jansen, A.J. Freeman, Total-energy full-potential linearized augmented-plane-wave method for bulk solids: Electronic and structural properties of tungsten, Physical Review B, 30 (1984) 561-569.
[80] L.F. Mattheiss, D.R. Hamann, Linear augmented-plane-wave calculation of the structural properties of bulk Cr, Mo, and W, Physical Review B, 33 (1986) 823-840.
[81] E. Lassner, W.-D. Schubert, The Element Tungsten, in: E. Lassner, W.-D. Schubert (Eds.) Tungsten: Properties, Chemistry, Technology of the Element, Alloys, and Chemical Compounds, Springer US, Boston, MA, 1999, pp. 1-59.
[82] K.L. Chopra, M.R. Randlett, R.H. Duff, Face-centered-cubic Tungsten Films Obtained by, Applied Physics Letters, 9 (1966) 402-405.
[83] S. Cazottes, Z.L. Zhang, R. Daniel, J.S. Chawla, D. Gall, G. Dehm, Structural characterization of a Cu/MgO(001) interface using CS-corrected HRTEM, Thin Solid Films, 519 (2010) 1662-1667.
[84] S. Lee, J. Jeong, Y. Kim, S.M. Han, D. Kiener, S.H. Oh, FIB-induced dislocations in Al submicron pillars: Annihilation by thermal annealing and effects on deformation behavior, Acta Materialia, 110 (2016) 283-294.

[85] H. Idrissi, S. Turner, M. Mitsuhara, B. Wang, S. Hata, M. Coulombier, J.-P. Raskin, T. Pardoen, G. Van Tendeloo, D. Schryvers, Point Defect Clusters and Dislocations in FIB Irradiated Nanocrystalline Aluminum Films: An Electron Tomography and Aberration-Corrected High-Resolution ADF-STEM Study, Microscopy and Microanalysis, 17 (2011) 983-990.
[86] F. Hüe, M. Hÿtch, H. Bender, F. Houdellier, A. Claverie, Direct Mapping of Strain in a Strained Silicon Transistor by High-Resolution Electron Microscopy, Physical Review Letters, 100 (2008) 156602.
[87] D.J. Eaglesham, H.-J. Gossmann, M. Cerullo, Limiting thickness h_{epi} for epitaxial growth and room-temperature Si growth on Si(100), Physical Review Letters, 65 (1990) 1227-1230.
[88] Z. Liliental-Weber, W. Swider, K.M. Yu, J. Kortright, F.W. Smith, A.R. Calawa, Breakdown of crystallinity in low-temperature-grown GaAs layers, Applied Physics Letters, 58 (1991) 2153-2155.
[89] E. Rudy, S. Windisch, J.R. Hoffman, in Ternary Phase Equilibria in Transition Metal-Boron-Carbon-Silicon Systems. Part I. Related Binary Systems (Report Aerojet-General Corporation) Volume. VI
[90] R.H. Willens, E. Buehler, The Superconductivity of the Monocarbides of Tungsten and Molybdenum, Applied Physics Letters, 7 (1965) 25-26.
[91] J. Robertson, Diamond-like amorphous carbon, Materials Science and Engineering: R: Reports, 37 (2002) 129-281.
[92] B. Bhattarai, A. Pandey, D.A. Drabold, Evolution of amorphous carbon across densities: An inferential study, Carbon, 131 (2018) 168-174.

Figures:

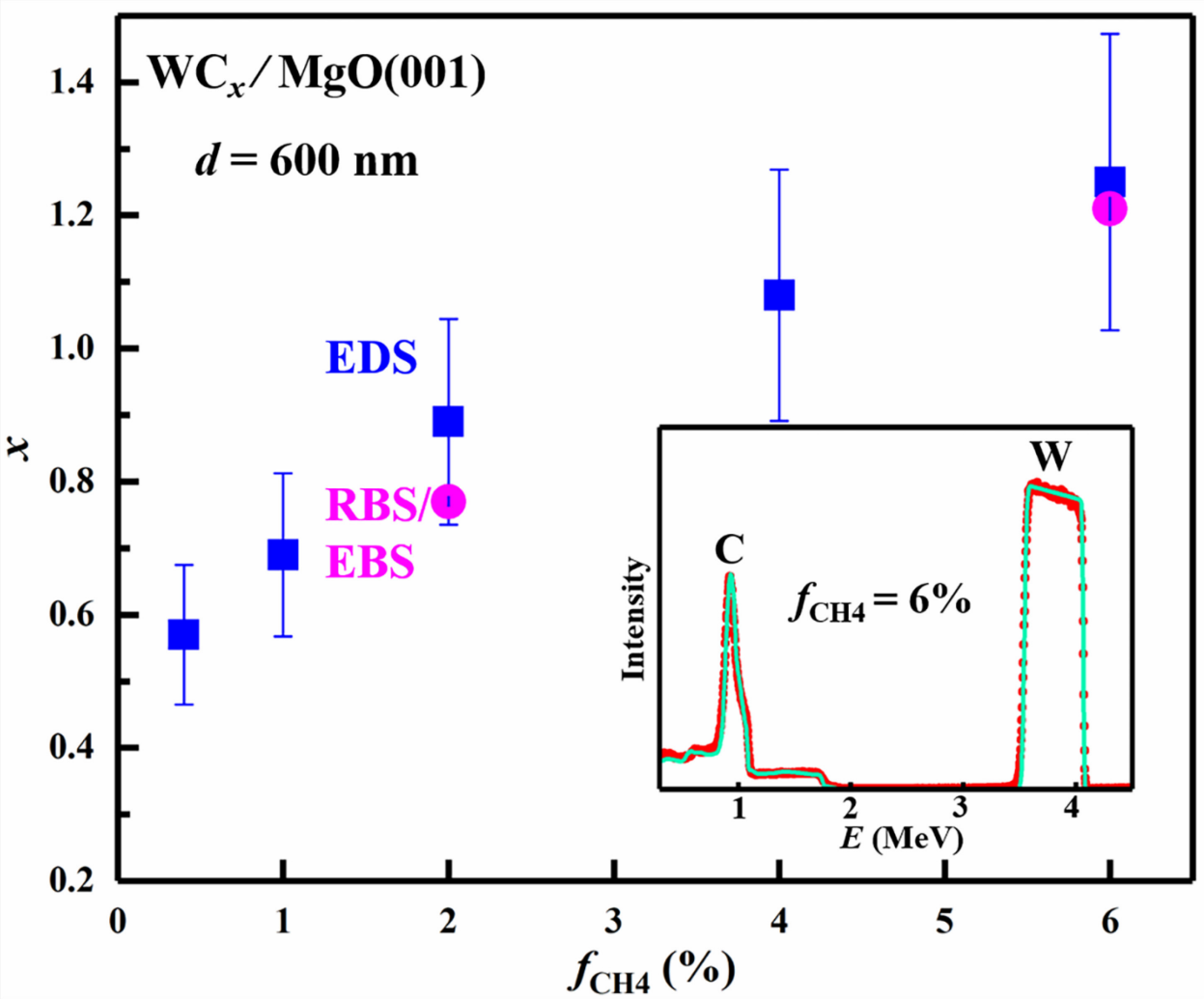

Fig. 1. The C-to-W ratio x vs the methane fraction f_{CH4} = 0.4 - 6% in the processing gas during reactive sputter deposition of 600-nm-thick WC_x layers, as measured by EDS (blue squares) and RBS/EBS (magenta circles). The inset shows a typical RBS/EBS spectrum including curve fitting for a layer with f_{CH4} = 6%.

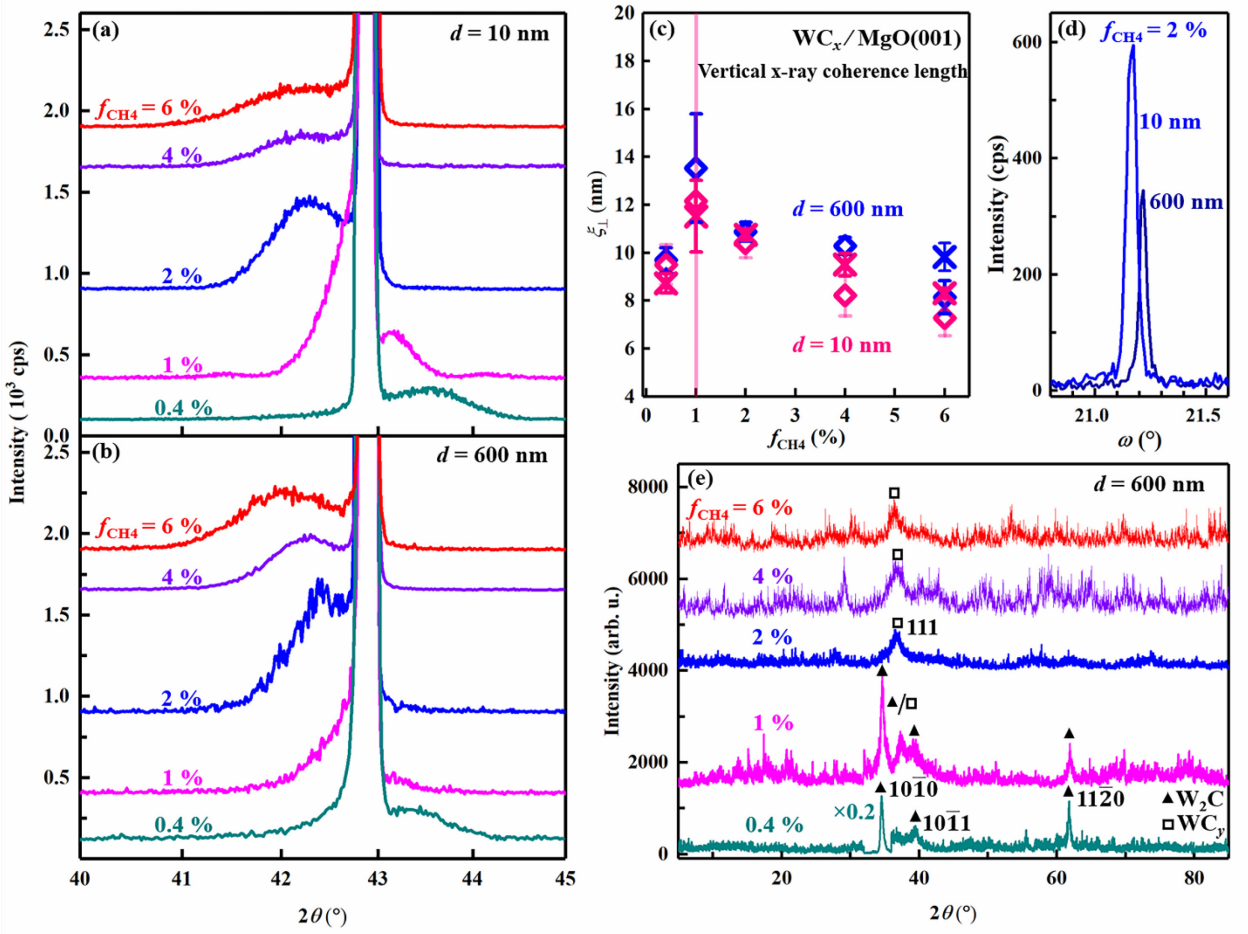

Fig. 2. X-ray diffraction θ-2θ scans for WC_x layers with thickness (a) d = 10 nm and (b) d = 600 nm. (c) The out-of-plane x-ray coherence length $\xi_\perp$ from d = 10 nm layers (pink) and d = 600 nm layers (blue), marked in diamond and cross symbols representing values obtained from ω-2θ scans and reciprocal space maps, respectively. (d) Typical ω-rocking curves from the 002 reflection of d = 10 and 600 nm layers with f_{CH4} = 2%. (e) Grazing incidence x-ray diffraction 2θ scans for d = 600 nm layers with f_{CH4} = 0.4-6%. Solid triangles and open squares denote peaks from hexagonal W_2C and cubic WC_y, respectively. The plotted intensity for f_{CH4} = 0.4% is reduced (0.2×) for 2θ = 32 – 36°.

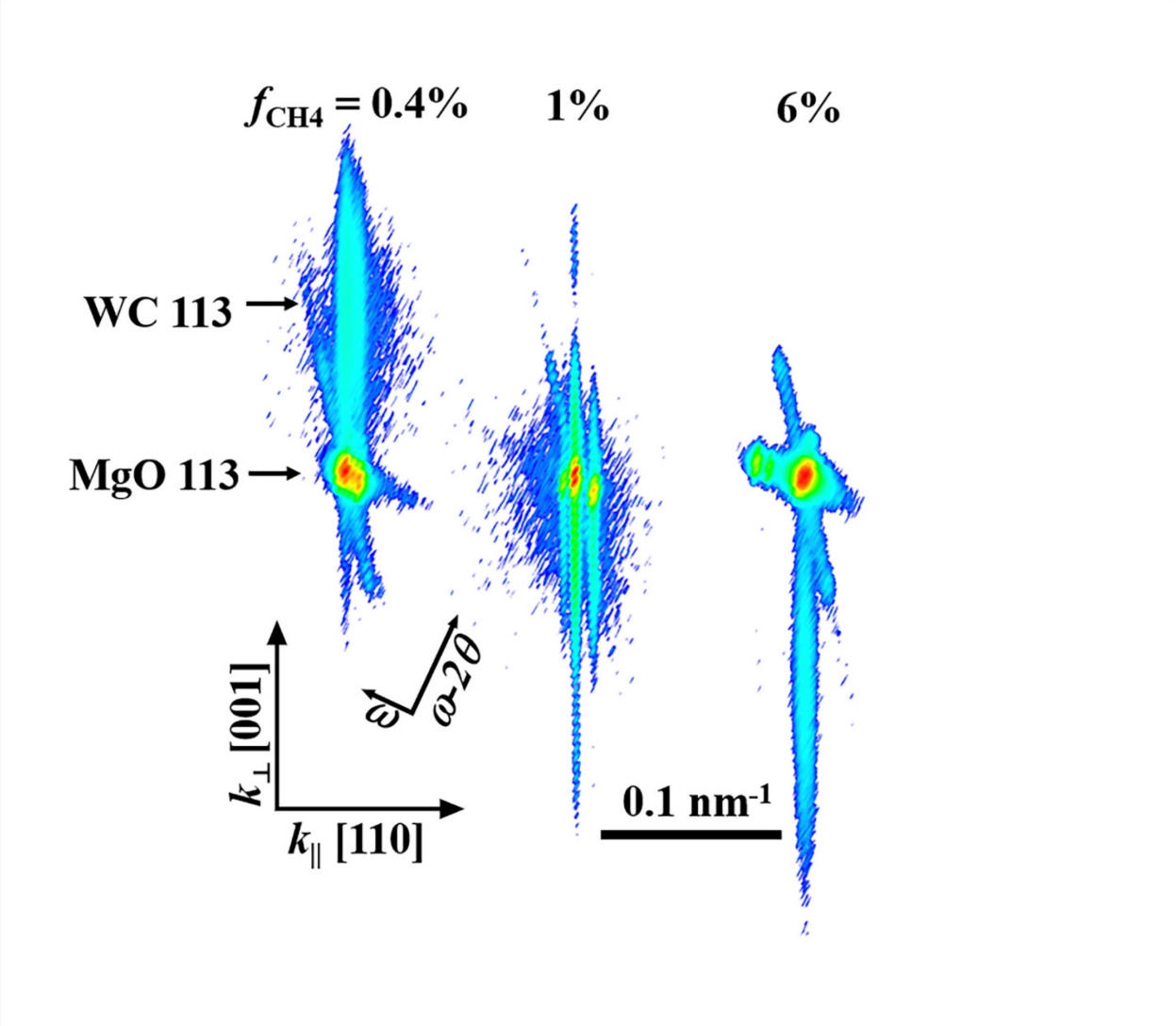

Fig. 3. XRD reciprocal space maps showing 113 reflections from 10-nm-thick WC_y(001)/MgO(001) layers deposited at f_{CH4} = 0.4% (left), 1% (center) and 6% (right).

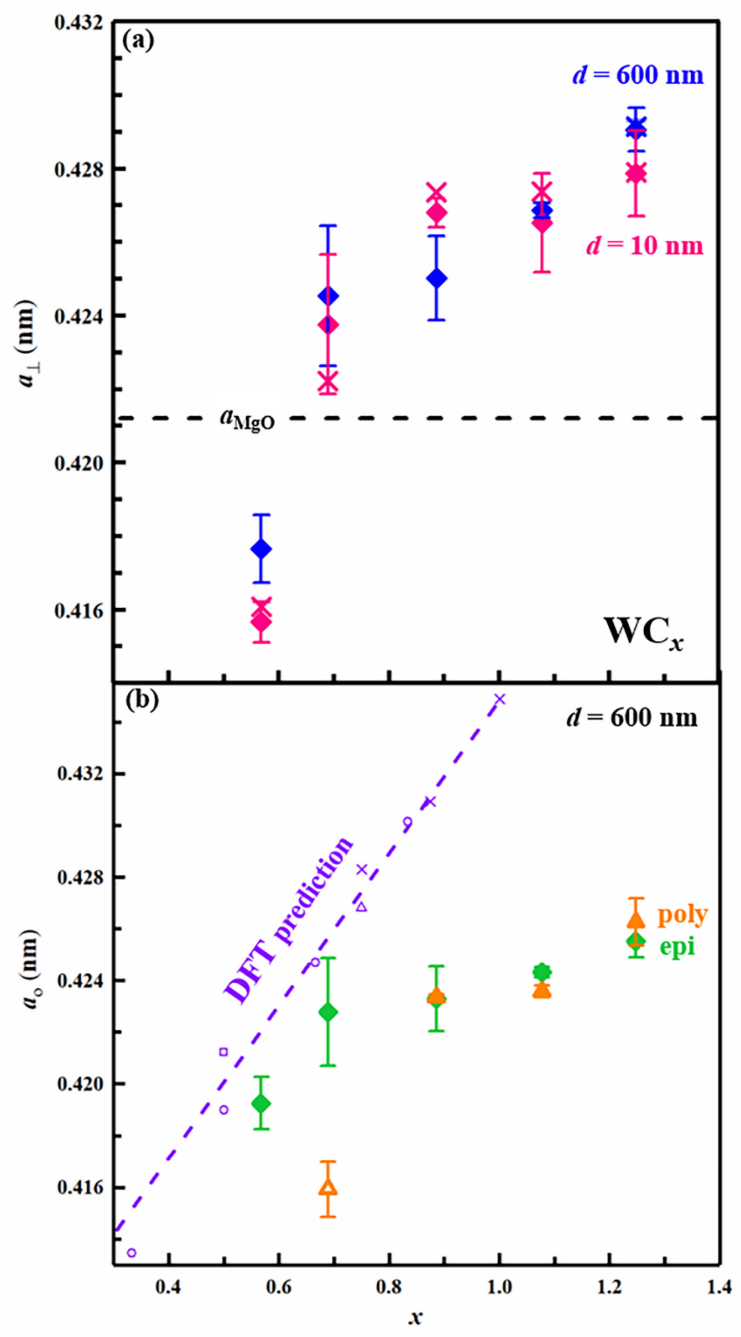

Fig. 4. (a) Out-of-plane lattice constant $a_\perp$ from RSMs (cross symbol) and θ-2θ scans (diamond) for d = 10 (pink) and 600 nm (blue) WC_x layers vs total C-to-W ratio x. (b) Relaxed lattice constant a_o from the epitaxial (green) and polycrystalline (orange) parts of 600-nm-thick WC_x layers. First-principles predictions (purple) of the lattice constant of cubic WC_y containing C vacancies on 111-planes (circles), 001-planes (square), along 110-lines (triangle), and on regular 3D arrays (crosses), and linear fit through the predicted values (dashed line).

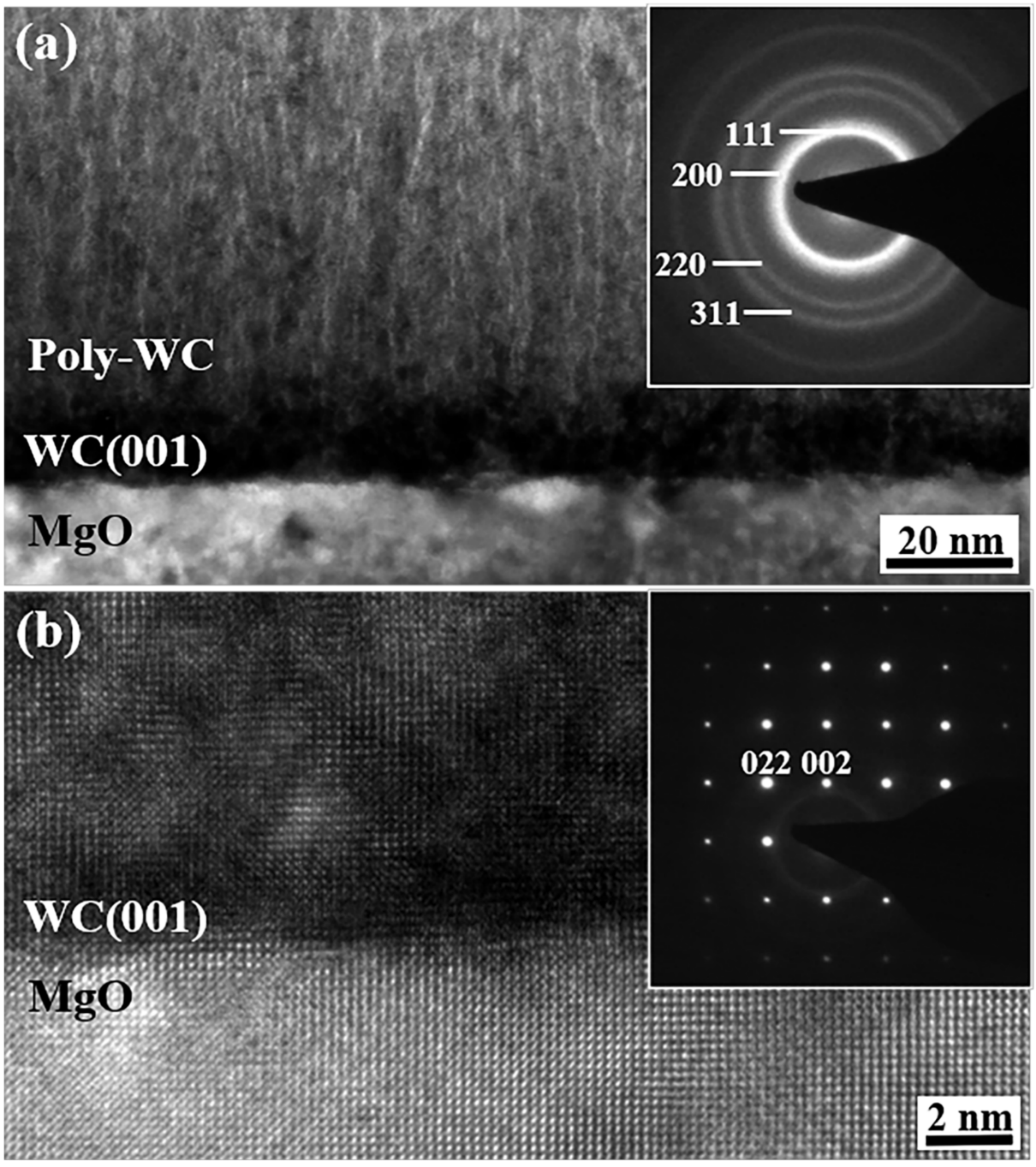

Fig. 5. TEM micrographs from a 600-nm-thick WC_x film deposited at f_{CH4} = 6%, showing (a) a low-magnification image of polycrystalline WC_x (incl. SAED pattern), epitaxial WC_y(001), and the MgO(001) substrate, and (b) a high-resolution micrograph with coherent lattice fringes near the epitaxial WC_y(001)/MgO(001) interface and a corresponding SAED pattern.

Table I. Total C-to-W ratio x in the tungsten carbide films measured by EDS, the carbon content y in the cubic WC_y lattice determined from XRD measurements and first-principle calculations, and the volume fraction $\%V_{a\text{-}C}$ of amorphous carbon (a-C:H) vs the methane fraction f_{CH4}. The superscripts *, † and # indicate the different methods for determining $\%V_{a\text{-}C}$, using the areal W density measured by RBS, assuming $\rho_{a\text{-}C}$ = 2 g/cm^3, and assuming stoichiometric W_2C, respectively.

f_{CH4} (%)	Total carbon content x in WC_x	Carbon content y in cubic WC_y	Amorphous carbon a-C:H volume fraction $\%V_{a\text{-}C}$
0.4	0.57	0.47	4%$^{\#}$
1	0.69	0.59	9%$^{\#}$
2	0.89	0.61	13%*, 13%†
4	1.08	0.64	19%†
6	1.25	0.68	26%*, 23%†